Bow Echo Mesovortices. Part I: Processes That Influence Their Damaging Potential

NOLAN T. ATKINS AND MICHAEL ST. LAURENT

Lyndon State College, Lyndonville, Vermont

(Manuscript received 13 May 2008, in final form 3 November 2008)

ABSTRACT

This two-part study examines the damaging potential and genesis of low-level, meso-γ-scale mesovortices formed within bow echoes. This was accomplished by analyzing quasi-idealized simulations of the 10 June 2003 Saint Louis bow echo event observed during the Bow Echo and Mesoscale Convective Vortex Experiment (BAMEX). This bow echo produced both damaging and nondamaging mesovortices. A series of sensitivity simulations were performed to assess the impact of low- and midlevel shear, cold-pool strength, and Coriolis forcing on mesovortex strength. By analyzing the amount of circulation, maximum vertical vorticity, and number of mesovortices produced at the lowest grid level, it was observed that more numerous and stronger mesovortices were formed when the low-level environmental shear nearly balanced the horizontal shear produced by the cold pool. As the magnitude of deeper layer shear increased, the number and strength of mesovortices increased. Larger Coriolis forcing and stronger cold pools also produced stronger mesovortices. Variability of ground-relative wind speeds produced by mesovortices was noted in many of the experiments. It was observed that the strongest ground-relative wind speeds were produced by mesovortices that formed near the descending rear-inflow jet (RIJ). The strongest surface winds were located on the southern periphery of the mesovortex and were created by the superposition of the RIJ and mesovortex flows. Mesovortices formed prior to RIJ genesis or north and south of the RIJ core produced weaker ground-relative wind speeds. The forecast implications of these results are discussed. The genesis of the mesovortices is discussed in Part II.

1. Introduction

Bow echoes are a well-known mode of severe convection that are capable of producing long straight-line wind damage swaths and tornadoes. Bow echo damage surveys (e.g., Fujita 1978, 1981; Fujita and Wakimoto 1981; Forbes and Wakimoto 1983; Atkins et al. 2005; Wheatley et al. 2006; Wakimoto et al. 2006a) have shown that the damage swaths can be up to a couple of hundred kilometers in length and commonly contain F0–F2 damage. Thus, it is not surprising that severe bow echo events have been responsible for significant property damage and loss of life (e.g., Fujita and Wakimoto 1981; Johns and Hirt 1987; Przybylinski 1995; Jorgensen and Weckwerth 2003; Atkins et al. 2004).

As first noted by Fujita (1978), it has long been hypothesized that bow echo damage swaths were created by a rear-inflow jet (RIJ) that descended to the ground from the rear of the convective system. The RIJ is a commonly observed system-scale feature in mesoscale convective systems (MCSs) and is generated by a midlevel horizontal buoyancy gradient formed as the convective system updraft tilts upshear and ascends rearward over the convective system's cold pool (Lafore and Moncrieff 1989; Weisman 1992). Doppler radar studies have documented the existence of RIJs at the apex of bow echoes (e.g., Forbes and Wakimoto 1983; Schmidt and Cotton 1989; Burgess and Smull 1990; Jorgensen and Smull 1993; Przybylinski 1995; Funk et al. 1999; Atkins et al. 2004). Wheatley et al. (2006) combined damage survey and radar data to confirm that bow echo damage swaths may be created by a descending RIJ.

Recent numerical and observational studies, however, have shown that low-level, meso-γ-scale (Orlanski 1975) ''mesovortices'' formed on the bow echo gust front are also capable of producing long swaths of straight-line wind damage. The generation of strong winds by bow echo mesovortices was first discussed in detail by Trapp and Weisman (2003). In their analysis of idealized bow echo simulations formed in moderate to

Corresponding author address: Nolan T. Atkins, Department of Meteorology, Lyndon State College, 1001 College Rd., Lyndonville, VT 05851.
E-mail: nolan.atkins@lyndonstate.edu

DOI: 10.1175/2008MWR2649.1

© 2009 American Meteorological Society

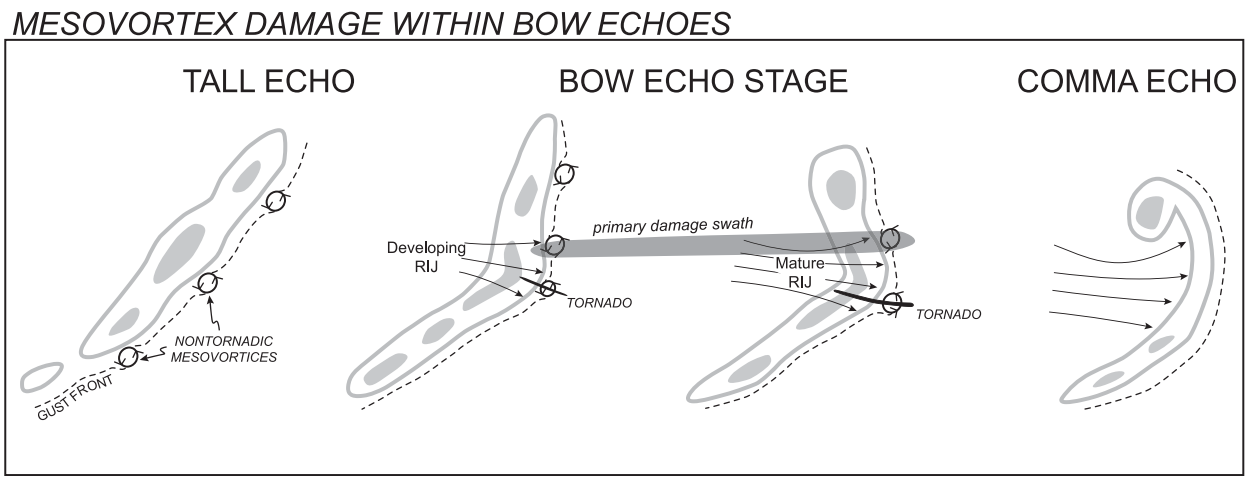

FIG. 1. Schematic diagram of a bow echo and attendant damage produced by mesovortices. Figure from Atkins et al. (2005).

strong low-level shear, it was shown that the strongest ground-relative winds were observed north of the bow echo apex and were associated with a mesovortex. The strong near-surface winds were generated by the horizontal pressure gradient created by the mesolow associated with the mesovortex via the fluid shear terms in the diagnostic perturbation pressure equation. Wakimoto et al. (2006b) analyzed a bow echo event on 6 July 2003 during the Bow Echo and Mesoscale Convective Vortex Experiment (BAMEX; Davis et al. 2004) utilizing airborne Doppler radar data. It was shown that the strongest ground-relative winds that produced F1 damage were located on the southern periphery of a mesovortex that was located just north of the descending RIJ. In contrast to the results shown by Trapp and Weisman (2003), the dual-Doppler data suggested that the damaging surface winds were created by a linear superposition of the vortex flow with the descending RIJ. Atkins et al. (2005) analyzed a bow echo event formed on 10 June 2003 during BAMEX over the greater Saint Louis, Missouri, area. By combining detailed damage survey and single-Doppler radar data, it was shown that a mesovortex created an 80-km-long straight-line wind damage swath located north of the bow echo apex, summarized in Fig. 1. The strongest winds were located on the southern periphery of the damaging vortex, consistent with the results of Wakimoto et al. (2006b). The association of straight-line wind damage swaths and mesovortices has also been shown by Wheatley et al. (2006).

Bow echoes are also well-known for spawning tornadoes (Fujita 1979; Forbes and Wakimoto 1983; Wakimoto 1983; Przybylinski 1995; Funk et al. 1999; Atkins et al. 2004; Atkins et al. 2005). Doppler radar studies have shown that mesovortices are often the parent tornadic circulation (e.g., Przybylinski 1995; Funk et al. 1999; Atkins et al. 2004, 2005). Bow echo tornadoes often form near the bow echo apex and often produce F0–F2 surface wind damage, however, they are capable of producing F3–F4 damage (Trapp et al. 2005).

Given the important role of mesovortices in producing straight-line wind and/or tornado damage within bow echoes, it is important to note that not all mesovortices are damaging. Distinguishing between stronger, damaging and weaker, nondamaging mesovortices has obvious and important severe-weather warning implications. Atkins et al. (2004, 2005) examined the structural differences between tornadic and nontornadic mesovortices in single-Doppler radar data. It was observed that tornadic mesovortices tended to be longer lived, deepened, and intensified rapidly just prior to tornadogenesis. The nontornadic mesovortices tended to be weaker, shallower, and shorter lived. Furthermore, Atkins et al. (2005) suggested a possible connection between the developing RIJ and tornadic mesovortices. As summarized in Fig. 1, their analysis showed that the tornadic mesovortices formed concurrently with or after the genesis of the RIJ and along the portion of the gust front strengthened by the RIJ. Nondamaging mesovortices were observed along the gust front both north and south of the RIJ. It was hypothesized that the RIJ locally deepened and strengthened the gust front. This would in turn lead to larger and deeper vortex stretching. The lack of high-resolution data, however, precluded testing this hypothesis.

Mesovortex evolution has been shown in idealized simulations to be sensitive to variations in environmental shear (Weisman and Trapp 2003) and Coriolis forcing (Trapp and Weisman 2003). Understanding

how different environmental conditions influence mesovortex evolution is important given the range of observed CAPE/shear environments that produce damaging convective wind events (Evans and Doswell 2001). A complete understanding of the dynamical processes that control mesovortex strength and, therefore, their damaging potential within bow echoes, remains elusive.

The primary objective of Part I of this study is, therefore, to better understand the environmental conditions and physical processes that control mesovortex strength and their damaging potential. This will be accomplished by analyzing quasi-idealized simulations of the 10 June 2003 bow echo documented by Atkins et al. (2005). Eleven mesovortices were observed with this event, five produced surface wind damage.

This paper is organized as follows. The experimental design is discussed in section 2. Section 3 presents results of sensitivity experiments on mesovortex strength while section 4 discusses the distinction between damaging and nondamaging mesovortices formed within the same bow echo. Conclusions are summarized in section 5. The genesis mechanisms of mesovortices are presented in Atkins and St. Laurent (2009, hereafter Part II).

2. Experimental design

All simulations presented herein were carried out with the Advanced Research Weather Research and Forecasting (ARW-WRF) model (Skamarock et al. 2005). The ARW model is a versatile, highly configurable mesoscale model that has been employed to simulate a wide variety of atmospheric phenomena. As described below, the ARW model was configured to perform quasi-idealized, three-dimensional, cloud-resolving simulations similar to those described by Weisman and Trapp (2003) and Trapp and Weisman (2003).

Computations were carried out on a model grid that was 225 and 320 km in size in the west–east and north–south directions, respectively, and was sufficiently large so that the simulated convective system did not propagate out of the model domain during the 6-h simulations. This could only be accomplished by subtracting a constant storm motion from the model wind profile to ensure that the convective system would stay approximately in the center of the model domain. In the vertical, the model domain extended up to 17.25 km. Both the system and subsystem-scale bow echo features were well resolved by the 750-m horizontal grid spacing. In the vertical, the grid spacing varied from 160 m near the ground to 600 m near the model top. The higher vertical grid resolution near the ground was necessary to well resolve the mesovortices and cold pool. The lateral boundary conditions were open. The upper and lower boundaries were rigid. A Rayleigh damping layer was placed above 12 km to suppress wave motions above the tropopause. The lower boundary condition was free slip and, therefore, will impact the low-level modeled wind field. Previous investigators (e.g., Lee and Wilhelmson 1997) have noted that frictional effects are important for simulating the detailed structure of small-scale vortices such as tornadoes. The results of Adlerman and Droegemeier (2002) and Weisman and Trapp (2003), however, suggest that the structural evolution of meso-γ-scale circulations such as mesovortices was not significantly impacted by the exclusion of surface friction. Convection was initiated in the model domain with three thermal bubbles 20 km apart oriented in the north–south direction. The Coriolis parameter was set to 1×10^{-4} s^{-1} and acted only on the wind perturbations. The 1.5 TKE closure scheme available in WRF was used to parameterize subgrid-scale turbulence, while the Lin et al. (1983) ice microphysics scheme was employed to parameterize microphysical processes.

The simulations presented herein should be considered ''quasi-idealized'' in that the model domain was initialized with the 1800 UTC 10 June 2003 Springfield, Missouri, sounding shown in Fig. 2. This sounding was launched in a high equivalent potential temperature air mass that appeared to be representative of the environment that spawned the Saint Louis bow echo. The sounding clearly shows an environment containing large convective available potential energy (CAPE) and moderate low-level wind shear of about 15 m s^{-1} concentrated in the lowest 2.5 km. Previous studies (e.g., Johns and Hirt 1987; Weisman 1993; Evans and Doswell 2001) have shown that bow echo environments are often characterized by large CAPE and moderate to strong low-level wind shear.

Relative to the idealized sounding used by Trapp and Weisman (2003), the Springfield sounding contains less 0–2.5-km shear (Fig. 2b) and is similar to the 15 m s^{-1}/2.5-km shear profile discussed in Weisman and Trapp (2003). The 0–2.5-km shear vector is westerly. The Springfield sounding also contains weak shear in the 2–5-km layer that strengthens farther aloft. The Weisman and Trapp (2003) sounding contains no shear above 2.5 km. The Springfield sounding has slightly larger CAPE and is drier at the low and midlevels (Fig. 2a) than the Weisman and Trapp (2003) sounding.

3. Sensitivity experiments

While previous modeling studies suggest that bow echo formation is favored in environments of large CAPE and moderate to strong low-level shear, the

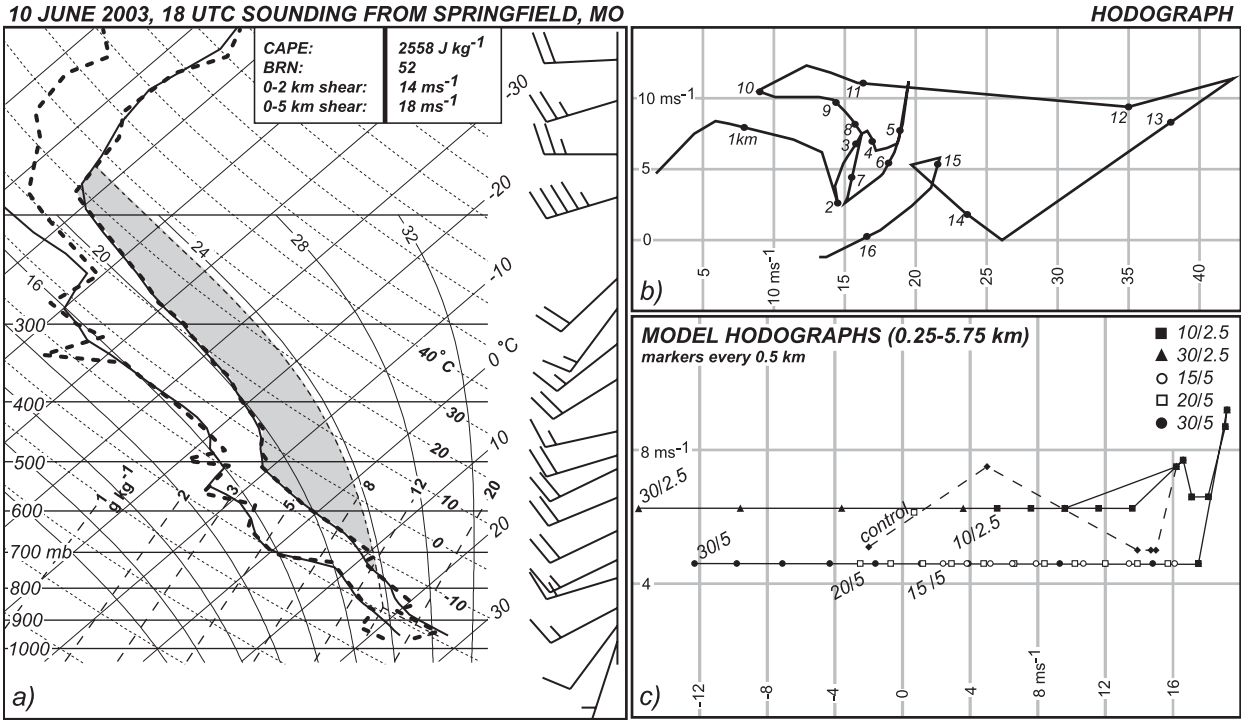

FIG. 2. (a) Skew T–log$p$ and (b) hodograph of the 1800 UTC 10 Jun 2003 Springfield, MO, sounding. The thick dashed lines in (a) are the observed temperature and dewpoint while the thin solid lines are the initial model temperature and dewpoint. The gray shaded area is the CAPE. Winds (half barb = 5 m s^{-1}; full barb = 10 m s^{-1}) are also shown. (c) Hodographs for the low-level and deep shear sensitivity experiments are shown over the lowest 5.75 km.

range of CAPE/shear values for bow echo environments has been observed to be quite large (Evans and Doswell 2001). Thus, it is important to understand how different environmental and convective system variations (e.g., cold-pool strength), may affect mesovortex evolution. Indeed, Weisman and Trapp (2003) showed that mesovortex strength was influenced by the magnitude of environmental shear and the Coriolis parameter. In this section, a series of sensitivity experiments are presented that examine the impact of low and midlevel shear, Coriolis forcing, and cold-pool strength on mesovortex strength and longevity. First, an overview of the control run is presented.

a. Control run

An overview of the control run (see Table 1) is shown in Fig. 3. By 2 h into the simulation, the three thermal bubbles had evolved into a continuous, linear convective line. Even at this pre–bow echo stage, both cyclonic and anticyclonic mesovortices had formed on the bow echo gust front. One hour later, the convective system had evolved into a bow echo with the RIJ and larger-scale bookend vortices (Weisman 1993) clearly evident. Cyclonic-only mesovortices were observed along the gust front at this time. The rainwater-mixing ratios along the leading edge of the bow echo were relatively small compared to those observed in the 20 m s^{-1}/2.5-km simulation shown by Weisman and Trapp (2003). This observation is attributed to the weaker low-level shear observed in the Springfield sounding. By 4 h into the simulation, the bow echo had grown up scale. The bookend vortices had moved rearward relative to the leading edge suggesting that the cold pool and attendant horizontal vorticity at its leading edge had overwhelmed the environmental horizontal vorticity (Weisman 1993). Cyclonic-only mesovortices were evident. The overall scale, orientation, and timing of the simulated MCS are qualitatively similar to the observed 10 June 2003 event.

A more detailed depiction of the mesovortices formed in the control run is shown in Fig. 4 where the gust front and mesovortex positions are shown every 20 min for the last 5 h of the simulation. The first mesovortices formed at about 80 min into the simulation, well before the convective system acquired bow echo characteristics. Interestingly, the initial mesovortices were only cyclonic. As the MCS evolved into a bow echo, both cyclonic and anticyclonic mesovortices

TABLE 1. Listing of all sensitivity runs. Here $\Delta\mathbf{U}$ is the wind shear within a given layer. The observed structure of the MCS during the mature stage is given as follows. Weak bow echo (WBE) simulations were characterized by substantially upshear tilted updrafts, shallow system-scale circulations, and relatively weak convective lines. Stronger BEs were characterized by deeper and stronger system-scale circulations and more intense convective lines. The WK simulations contained scattered cells well behind the gust front and weak or nonexistent system-scale circulations. The LIN simulation remained a small-scale linear convective system. The numbers in parentheses refer to the respective sensitivity simulation.

Expt type	Depth of $\Delta\mathbf{U}$ (km)	$\Delta\mathbf{U}$ (m s^{-1})	Microphysics scheme	f ($\times 10^{-4}$ s^{-1})	Mature mode
Control	2.5, 5.0	18, 22	Lin et al.	1	WBE
Low-level shear	2.5	10, 30	Lin et al.	1	WK(10), BE(30)
Midlevel shear	5.0	15, 20, 30	Lin et al.	1	WK(15), WK(20), BE(30)
Coriolis	Same as control	Same as control	Lin et al.	0.01, 1, 2	WBE(0.01), WBE(1), WBE(2)
Cold-pool strength	Same as control	Same as control	Kessler:		
			Evaporation rate = 100%	1	WBE/BE(100%)
			Evaporation rate = 50%		WBE(50%)
			Evaporation = 25%		LIN(25%)

formed. With time, however, only cyclonic mesovortices were again observed. The cyclonic mesovortices observed later in the simulation tended to be larger, stronger, and longer lived than those observed earlier. Mesovortices were often observed to become larger through the action of merging with like-signed vortices, consistent with the results of Lee and Wilhelmson (1997) and Trapp and Weisman (2003).

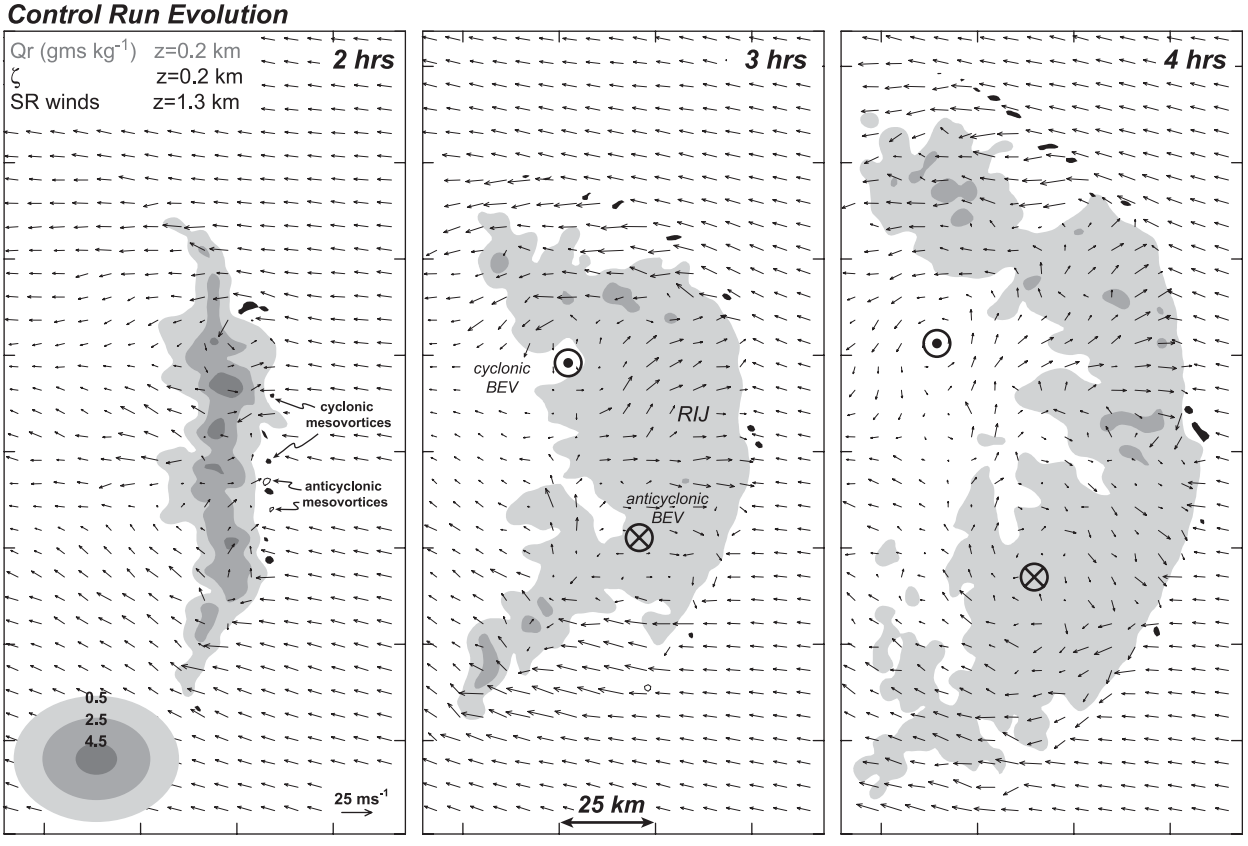

FIG. 3. Evolution of the control run at 2, 3, and 4 h into the simulation. Rainwater mixing ratio (g kg^{-1}) is shaded gray. Locations of cyclonic mesovortices where the vertical vorticity is greater than 1.25×10^{-2} s^{-1} are filled in black. The thin black contours are locations of anticyclonic mesovortices having vertical vorticity values less than -1.25×10^{-2} s^{-1}. The positions of the cyclonic and anticyclonic bookend vortices are shown at 3 and 4 h. Storm-relative winds at 1.3 km are plotted at all times.

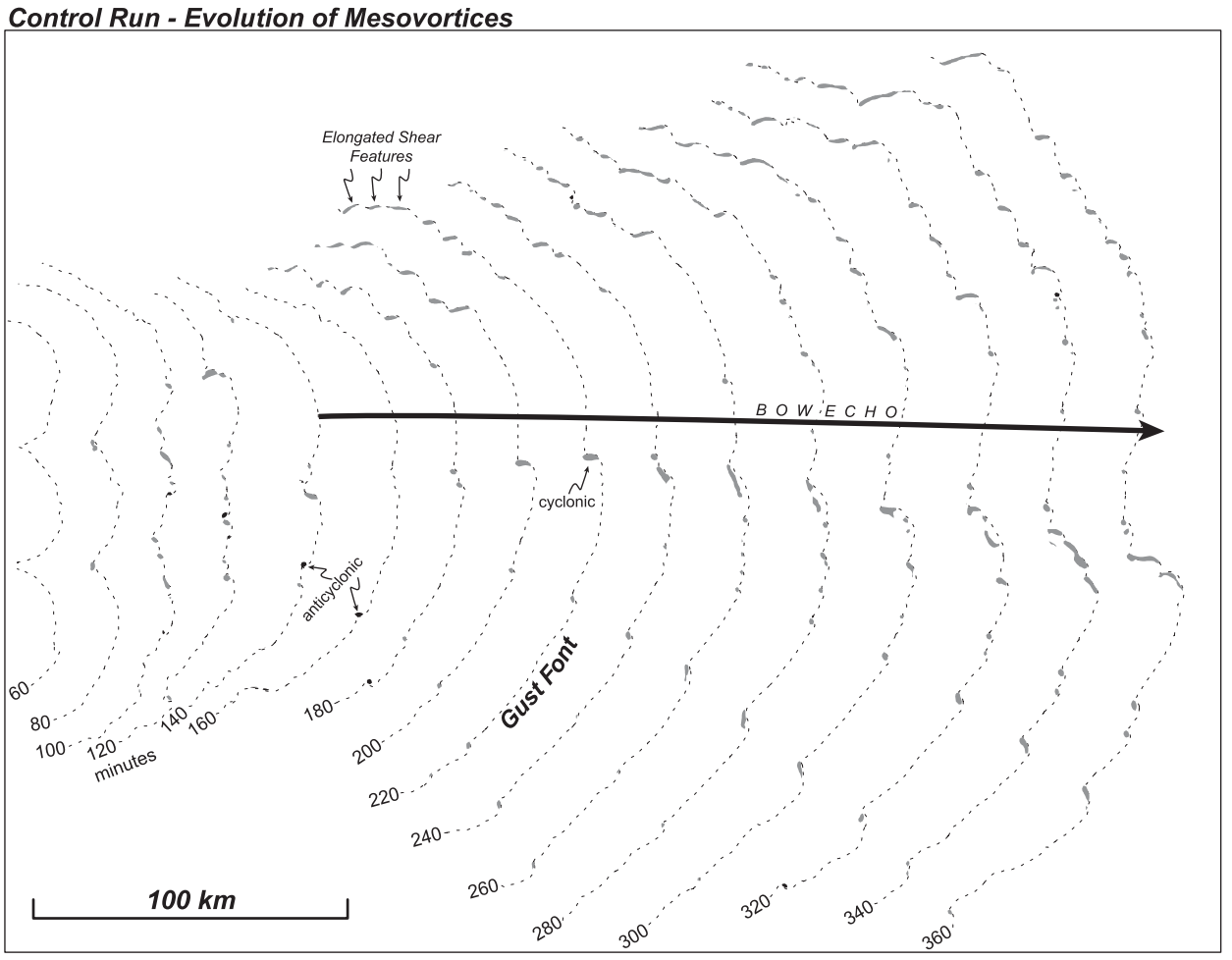

FIG. 4. Gust front (dashed line) and mesovortex locations are plotted for the control run from 60 to 360 min, every 20 min at 0.2 km. The gust front position delineates the eastern edge of the cold pool defined as the −1°C perturbation from the base state at 0.2 km. Cyclonic and anticyclonic mesovortex locations are filled gray and black, respectively, and are located in a similar manner as in Fig. 3.

The genesis mechanisms of the mesovortics shown in Fig. 4 appeared to be different than what was described by Trapp and Weisman (2003). They showed that mesovortices formed in anticyclonic–cyclonic pairs through downward tilting of baroclinically generated horizontal vortex lines by rainy downdrafts thus producing an anticyclonic vortex to the north of the cyclonic circulation. In contrast, *cyclonic-only* mesovortices formed in Fig. 3 along with vortex pairs with *cyclonic* circulation observed to the north of the anticyclonic circulation. The mesovortex genesis mechanisms are discussed in Part II.

b. The sensitivity experiments

The different sensitivity experiments are summarized in Table 1. The range of convective organization observed during the mature stage varied from disorganized convective systems (WK) to strong bow echoes (BE) with a small-scale linear system (LIN) observed in the weakest cold-pool strength simulation. The results of the sensitivity experiments are shown in Fig. 5 where the time series of circulation at the lowest grid level (82 m) was plotted as a function of time. The circulation was computed as $\Gamma = \Sigma\bar{\zeta}A$ where $\bar{\zeta}$ is the mean vertical vorticity within some area A, and the sum is over all mesovortices. The area A is defined as the area of the mesovortex containing vertical vorticity values greater than $1.25 \times 10^{-2}\ \mathrm{s}^{-1}$ for all positive vortices. This vertical vorticity threshold was subjectively determined and appeared to well distinguish coherent mesovortices from weaker, transient features. Since it was often difficult to distinguish between mesovortices and elongated shear features that were commonly observed along the northern portion of the MCS (see Fig. 4), the circulation sum

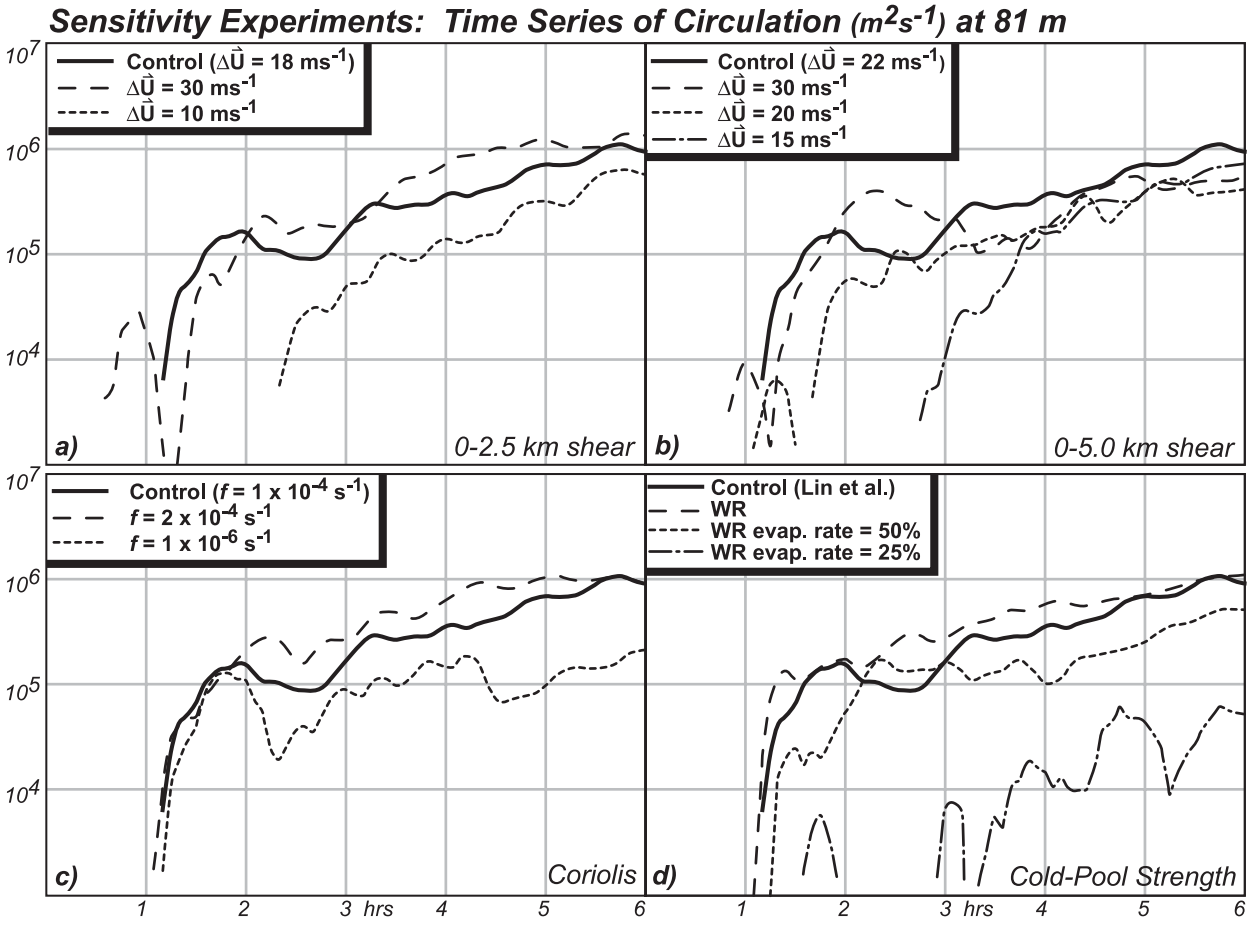

FIG. 5. Time series of circulation ($m^2 s^{-1}$) calculated at the lowest model grid level (81 m) for the different sensitivity experiments. The sensitivity experiments include (a) low-level shear, (b) deep shear, (c) Coriolis forcing, and (d) cold-pool strength. The thick solid line in (a)–(d) represents the control run.

was over all nonzero area that met the vertical vorticity threshold and, therefore, included the enhanced shear features. Thus, the time series plots in Fig. 5 *approximately* represent the total circulation produced at the lowest model grid level by mesovortices. Finally, only plots of positive circulation are shown since the number of anticyclonic mesovortices was quite small in the control run (Fig. 4) and all of the sensitivity simulations.

Results of the low-level shear experiments are shown in Fig. 5a (see Fig. 2c for the 0.25–5.75-km hodographs for all shear sensitivity experiments). Relative to the control run where $\Delta\mathbf{U}$, the wind shear over the lowest 2.5 km, was approximately 15 m s^{-1}, weaker (stronger) low-level shear produced less (more) circulation at low levels. Circulation appeared later in the weaker shear simulation. The larger circulation observed in the stronger shear simulation can be attributed to both stronger mesovortices (Fig. 6a) and more of them for the first 5 h of the simulation (Fig. 6b). In all simulations, the circulation increased with time. This was due to a slight strengthening of mesovortices (Fig. 6a) and a noticeable increase of mesovortex numbers with time (Fig. 6b). The increasing number of mesovortices with time was attributed to cold-pool expansion producing a larger number of mesovortex generation sites along the gust front (Figs. 3 and 4).

The more intense mesovortices observed in the stronger low-level shear simulation can be explained with the cold-pool shear balance theory for long-lived squall lines originally discussed by Rotunno et al. (1988). The cold-pool intensity C, is approximated by

$$C^2 = 2\int_0^H (-B)dz, \tag{1}$$

where B and H are the cold-pool buoyancy and depth, respectively. When the magnitude of C is approximately equal to the wind shear normal to the convective line

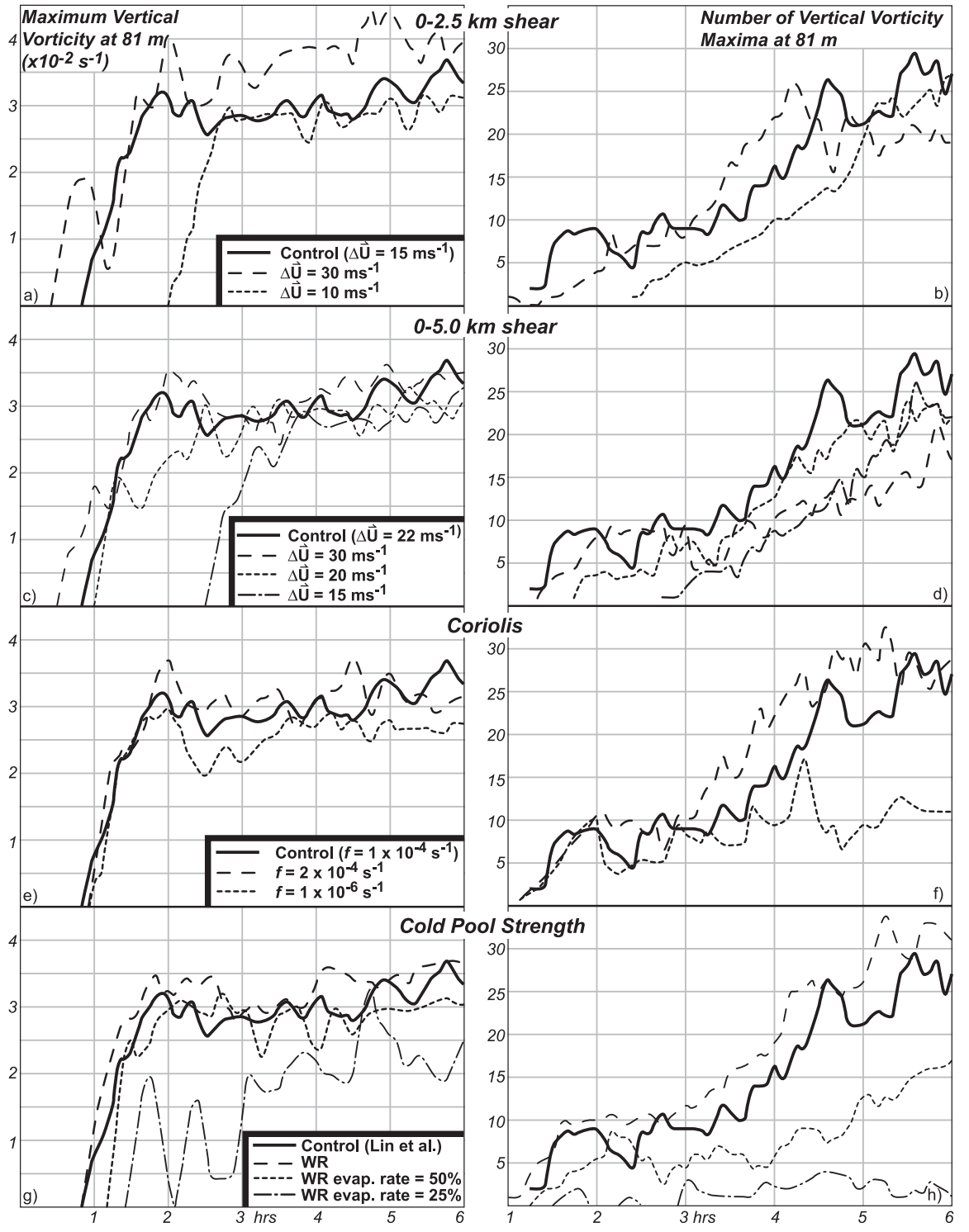

FIG. 6. (a),(c),(e),(g) Time series of maximum vertical vorticity and (b),(d),(f),(h) number of vertical vorticity maxima at 81 m for all of the sensitivity experiments shown in Fig. 5. Similar to the circulation analysis in Fig. 5, a vertical vorticity threshold of $1.25 \times 10^{-2}\ s^{-1}$ was used when determining the number of vertical vorticity maxima.

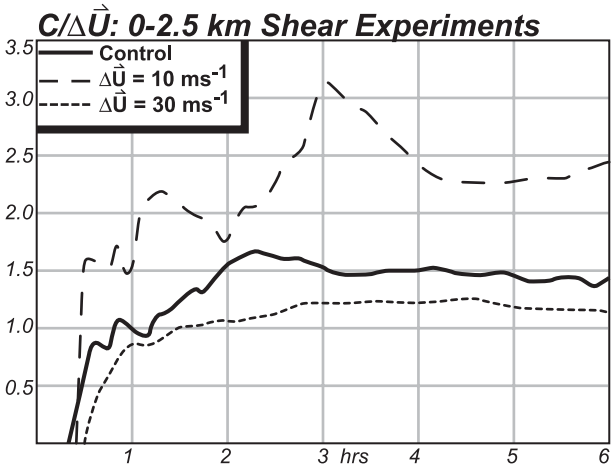

FIG. 7. Time series of $C/\Delta\mathbf{U}$ for the low-level (0–2.5 km) shear experiments shown in Fig. 5. Both C and $\Delta\mathbf{U}$ are defined in the text.

orientation and over the depth of the cold pool ($\Delta\mathbf{U}$), the horizontal vorticity produced by the environmental shear and cold pool will balance each other resulting in upright, deep updrafts and deeper and stronger vortex stretching. When $C/\Delta\mathbf{U} < 1$, the updrafts will tilt downshear. Likewise, if $C/\Delta\mathbf{U} > 1$, the updrafts will tilt upshear.

Time series of $C/\Delta\mathbf{U}$ for the three low-level shear experiments in Fig. 5a are shown in Fig. 7. The cold-pool and low-level shear were in approximate balance for the $\Delta\mathbf{U} = 30$ m s^{-1} simulation with C slightly larger than $\Delta\mathbf{U}$. As the low-level shear decreased, $C/\Delta\mathbf{U}$ increased. Thus, the $\Delta\mathbf{U} = 30$ m s^{-1} simulation would be associated with stronger, upright updrafts at the leading edge of the convective system relative to the weaker shear simulations. Therefore, vertical vortex stretching would be largest in this simulation. Visual inspection of the stretching tendency term confirmed this hypothesis (not shown). Thus, consistent with the circulation time series in Fig. 5a and maximum vertical vorticity in Fig. 6a, the strongest mesovortices would be formed when $C/\Delta\mathbf{U}$ is just greater than 1, suggesting that the convective system is weakly tilted upshear. The vortices in the $\Delta\mathbf{U} = 30$ m s^{-1} simulation were also longer lived than in the control or $\Delta\mathbf{U} = 10$ m s^{-1} simulation (not shown).

Similar to the low-level shear experiments, mesovortex production was delayed as the magnitude of deep shear decreased (Fig. 5b). Furthermore, the amount of circulation produced in the first 4 h decreased as the shear magnitude decreased. Circulation magnitudes were similar for all deep-shear runs after 4 h. Mesovortex strength generally increased as the deep-shear magnitude increased (Fig. 6c). Similar behavior was observed in the low-level shear experiments (Fig. 6a). Generally, the number of mesovortices increased as the deep-shear magnitude became larger. The exception was the $\Delta\mathbf{U} = 30$ m s^{-1} run where the number of mesovortices during the latter part of the simulation was less than the other deep-shear experiments. Interestingly, similar behavior was observed in the low-level shear experiments and was attributed to the merger of like-signed vortices observed later in the simulation.

The magnitude of Coriolis forcing had an impact on low-level circulation production by mesovortices (Fig. 5c). Relative to the control ($f = 1 \times 10^{-4}$ s^{-1}), weaker (stronger) Coriolis forcing produced less (more) low-level circulation. Somewhat stronger mesovortices were produced with larger Coriolis forcing (Fig. 6e). The number of mesovortices depended strongly on the magnitude of Coriolis forcing (Fig. 6f). Relative to the control, stronger (weaker) Coriolis forcing produced more (less) mesovortices, particularly after 2 h into the simulation. The difference in mesovortex numbers became more noticeable after 4 h. These results suggest that Coriolis forcing plays a role in mesovortex evolution, consistent with the results of Trapp and Weisman (2003). Trapp and Weisman (2003) showed that stretching of planetary vorticity is an important contributor to the amplification of cyclonic mesovortices. They also observed fewer mesovortices when Coriolis forcing was set to zero.

Results for the cold-pool strength experiments are shown in Fig. 5d. The control run, utilizing the Lin ice microphysics scheme, was compared to simulations using the Kessler warm rain scheme where the evaporation rate was successively decreased to 50 and 25% of its actual value. The smaller evaporation rates resulted in weaker (as measured by potential temperature or buoyancy perturbations) and smaller cold pools. The results in Fig. 5d show that weaker and smaller cold pools produced less mesovortex circulation. The mesovortices formed in the weaker cold-pool simulations were somewhat weaker (Fig. 6g) owing to weaker convergence and vertical vortex stretching along the gust front (not shown). More significantly, the number of mesovortices formed were much less as the cold-pool strength decreased (Fig. 6h). Weaker cold pools will expand horizontally at a slower rate resulting in spatially smaller convective systems. This result is shown in Fig. 8 where the fraction of the horizontal domain at 81 m covered by the cold pool is plotted for the same experiments in Fig. 5d. Clearly, as the cold-pool strength weakened, its size decreased. Therefore, fewer mesovortices formed (Fig. 6h) simply because there were fewer mesovortex initiation sites on the leading edge of the smaller convective system.

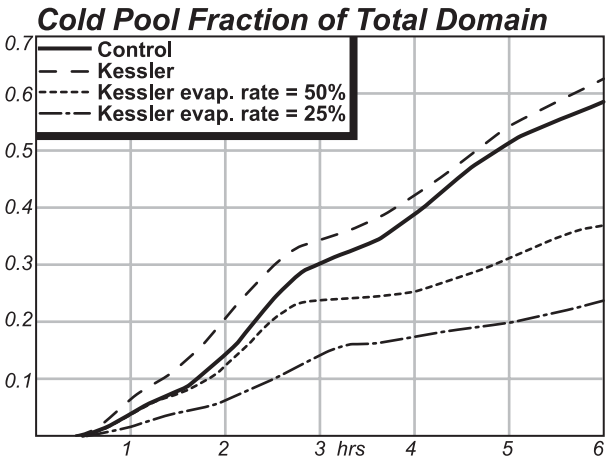

FIG. 8. Time series of cold-pool fraction (%) of the total domain for the cold-pool strength sensitivity experiments shown in Fig. 5. Similar to Fig. 4, the cold pool was defined as the −1°C perturbation from the base state at 0.2 km.

4. Generation of damaging surface winds

A growing number of studies have shown that mesovortices are important for producing wind damage within bow echoes. Atkins et al. (2005), however, showed that not all mesovortices observed within the 10 June 2003 Saint Louis bow echo were damaging. Analysis of damage survey and single-Doppler radar data suggested that the damaging vortices formed coincident and after the genesis of the RIJ and along the portion of the gust front that was strengthened by the descending RIJ. Atkins et al. (2005) hypothesized that vortex stretching was locally stronger and deeper along the gust front enhanced by the RIJ. Wakimoto et al. (2006b) showed that an F1 surface wind damage swath was produced by enhanced winds on the southern flank of a mesovortex formed near the bow echo apex. In this section, the relationship between the RIJ, mesovortices, and strong surface winds is examined.

Results from the $\Delta\mathbf{U} = 30$ m s^{-1} over 2.5-km experiment are presented in Fig. 9 and are generally representative of the relationship between the RIJ, mesovortices, and damaging surface winds observed in many of the other sensitivity experiments discussed in section 3. Generally, the near-surface ground-relative winds (GRWS) weakened as the shear magnitude and cold-pool strength became smaller. At 180 min (Fig. 9a), the near-surface GRWS were generally less than 35 m s^{-1}. Local maxima in near-surface GRWS were generally associated with mesovortices along the leading edge of the convective system. No well-defined RIJ had yet formed. Twenty minutes later (Fig. 9b), the RIJ at 1.5 km was becoming evident in the wind field. It was also observed in the vertical cross section in Fig. 10a at low–midlevels with 30–35 m s^{-1} of ground-relative flow well behind the surface gust front position. The near-surface GRWS had not increased since 180 min. By 220 min (Figs. 9c and 10b) the RIJ had clearly strengthened. The RIJ had also begun to descend to the surface just behind the gust front (Fig. 10b). The near-surface GRWS increased slightly in magnitude since 200 min. Notice that mesovortices were observed south of, along, and north of the developing RIJ. By 240 min, the RIJ had continued to strengthen, expand rearward, and was descending to the surface just behind the gust front (Figs. 9d and 10c). The near-surface GRWS had increased dramatically with a local maximum in excess of 45 m s^{-1} located on the southern flank of a strengthening mesovortex that was about to undergo a merger. The mesovortex was also located along the gust front that was being enhanced by the developing RIJ. The near-surface GRWS increased to near 50 m s^{-1} by 260 min with the maximum located on the southwestern flank of the merged vortex. The merged vortex was located near and just north of the RIJ core that had continued to strengthen (Figs. 9e and 10d). Weaker mesovortices associated with weaker local maxima in near-surface GRWS were located both north and south of the RIJ and merged mesovortex. For example, mesovortices 1 and 7 were associated with near-surface GRWS of approximately 24 and 28 m s^{-1}, respectively. Consistent with Fig. 9e, Figs. 11a,b clearly show the absence of a RIJ near mesovortices 1 and 7. The larger merged vortex continued to produce strong near-surface GRWS at 280 min (Fig. 9f). Interestingly, two additional maxima in near-surface GRWS were observed with mesovortices 2 and 4, which have also increased in strength since 260 min. Similar to the larger merged mesovortex, enhanced rear inflow was observed just south of mesovortices 2 and 4. All of the other weaker mesovortices (1, 5, and 7) were associated with much weaker near-surface GRWS and were not located near a RIJ.

The analyses shown in Figs. 9–11 showed that the strongest near-surface GRWS were found on the southern flank of a strengthening mesovortex that was located near or just north of the RIJ core that descended to the surface. Weaker maxima in near-surface GRWS were associated with mesovortices formed prior to RIJ genesis or north and south of the RIJ position. These results are consistent with those discussed by Atkins et al. (2005) and suggest a combination of RIJ and mesovortex flows may be important in creating strong local maxima in near-surface GRWS. Exactly how the RIJ and mesovortex create strong local maxima in near-surface GRWS is now discussed.

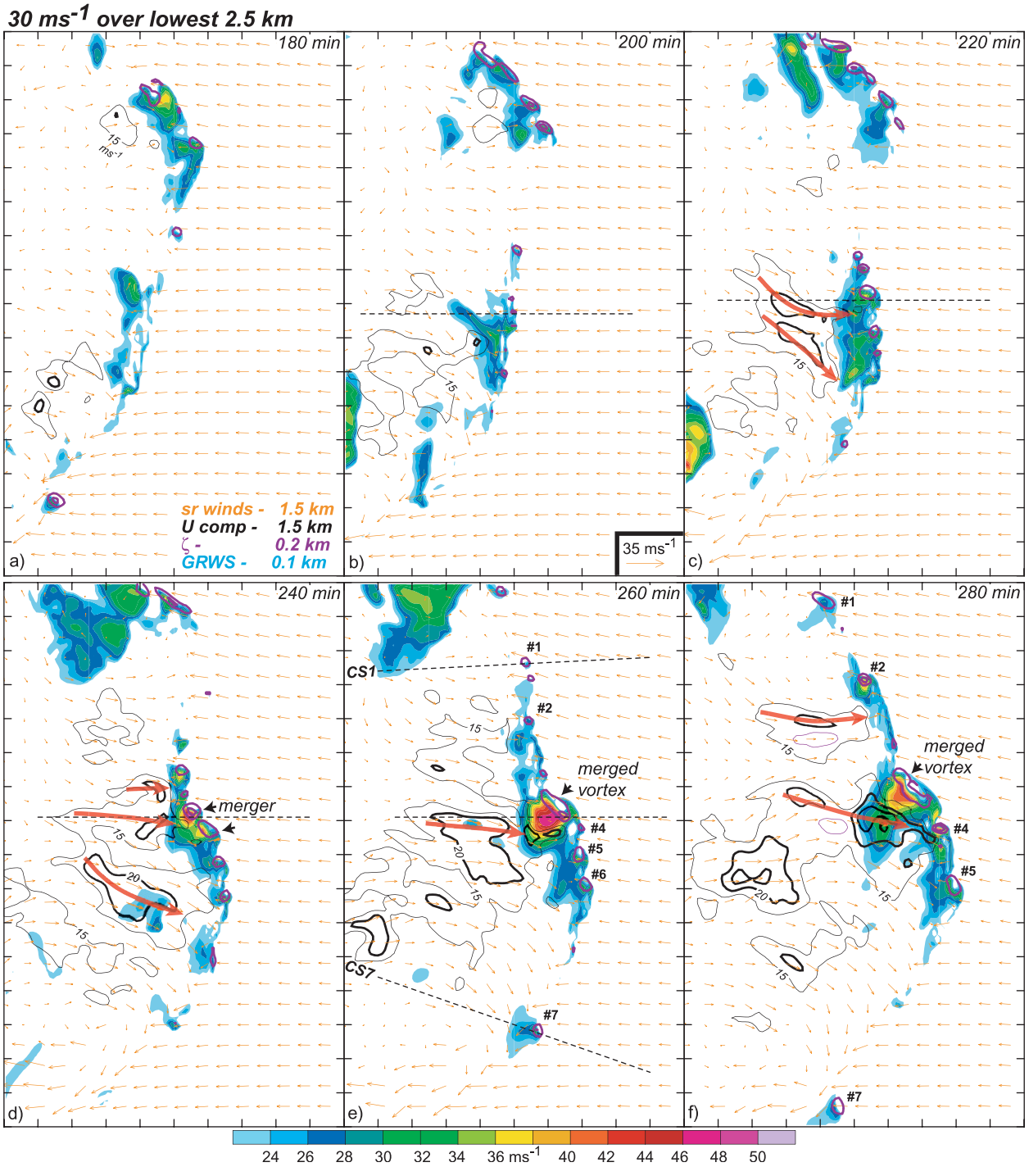

FIG. 9. Time series from 180–280 min of GRWS (m s^{-1}), storm-relative winds (vectors, m s^{-1}), U component of the storm-relative flow (black contours, m s^{-1}), and vertical vorticity (purple contours, $\times 10^{-2}$ s^{-1}) for the $\Delta\mathbf{U} = 30$ m s^{-1} low-level shear experiment. Vertical vorticity is contoured beginning at 1.25×10^{-2} s^{-1}, every 2×10^{-2} s^{-1}. The heights of the displayed fields are shown in (a). Individual mesovortex labels are shown in (d)–(f). The thick red arrows represent approximate RIJ core locations. Dashed lines are cross-section locations shown in Figs. 10 and 11.

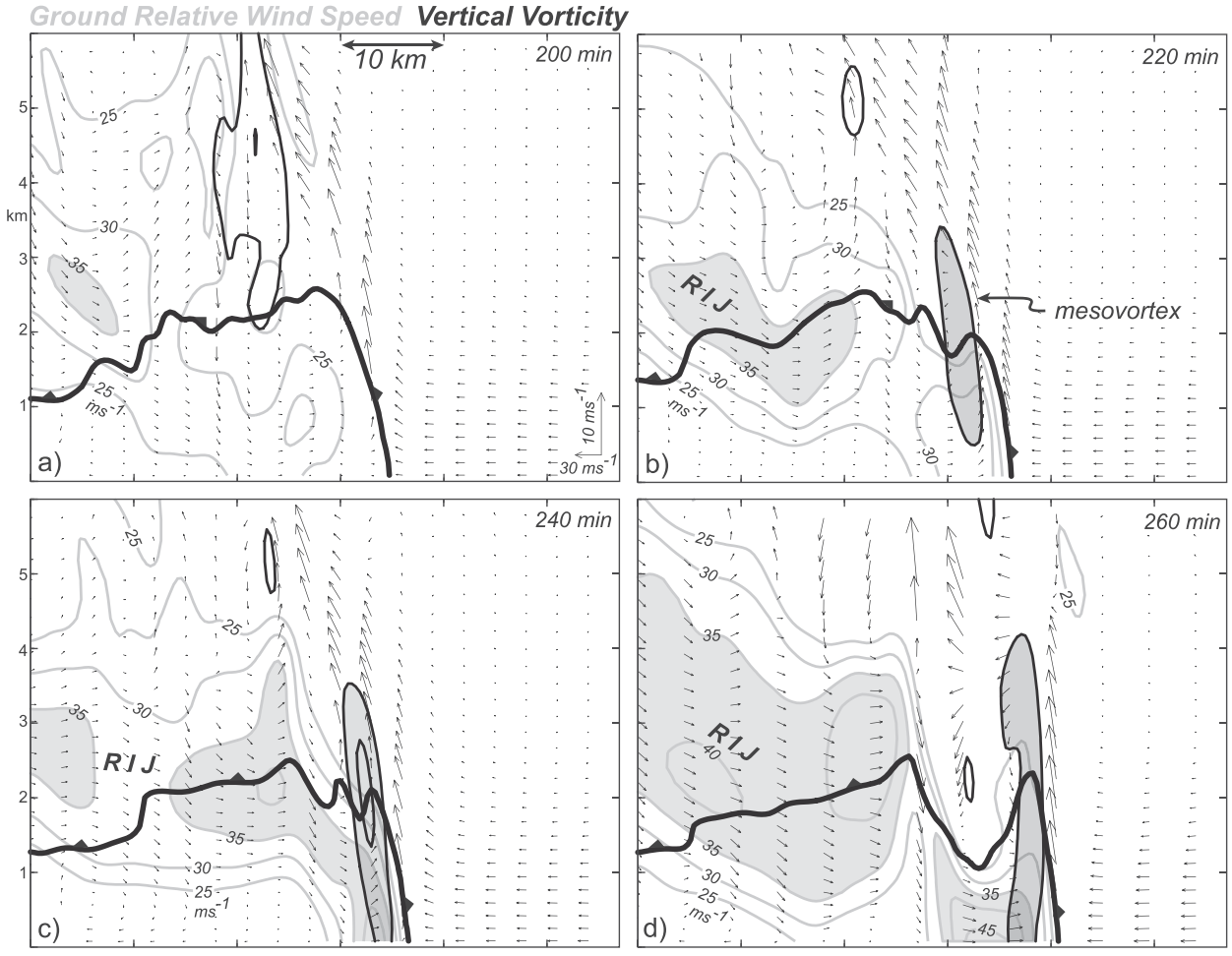

FIG. 10. Vertical cross sections through the bow echo gust front at 200, 220, 240, and 260 min. Cross-section locations are shown in Fig. 9 at the respective times. The gust front location is shown at the thick black line and delineates the 299-K potential temperature isotherm. Storm-relative winds (m s^{-1}) in the plane of the cross section are shown in the vector field. Gray contours are GRWS (m s^{-1}) in the plane of the cross section. Vertical vorticity, contoured as in Fig. 9, is shown in thin black contours. Mesovortices are lightly shaded gray.

The fact that the near-surface GRWS maxima were observed on the southern flank of the mesovortices suggested that they were created by a linear superposition of vortex flow and the translational motion of the flow within which the vortex was embedded. This type of flow asymmetry is commonly observed in translating tornadoes and hurricanes and is evident in poststorm damage surveys (e.g., Shea and Gray 1973; Fujita 1981; Wakimoto and Black 1994). Wakimoto et al. (2006b) observed a similar pattern in the flow field created by a bow echo mesovortex that generated F1 surface wind damage by analyzing dual-Doppler airborne radar data. By extracting the nondivergent horizontal flow due to the mesovortex, Wakimoto et al. (2006b) concluded that the strongest near-surface GRWS were created by the superposition of the vortex flow and the ambient flow within which the vortex was embedded. This result suggests that the strongest near-surface GRWS would be produced by strengthening mesovortices that are collocated with a descending RIJ. This hypothesis is explored for three of the mesovortices shown in Fig. 9e.

Assuming that the mesovortex flow is two-dimensional and nondivergent, the Poisson equation for the perturbation streamfunction, $\nabla^2\psi' = \zeta$ can be solved assuming that the vertical vorticity and perturbation streamfunction are zero at the lateral boundaries of the analysis domain. The retrieved streamfunction can then be used to compute the two-dimensional, nondivergent flow generated by the mesovortex.

This analysis was applied to the merged mesovortex and is shown in Fig. 12. The local maxima in GRWS of approximately 45–49 m s^{-1} was located just south of the merged mesovortex (Fig. 12a). The flow due to the

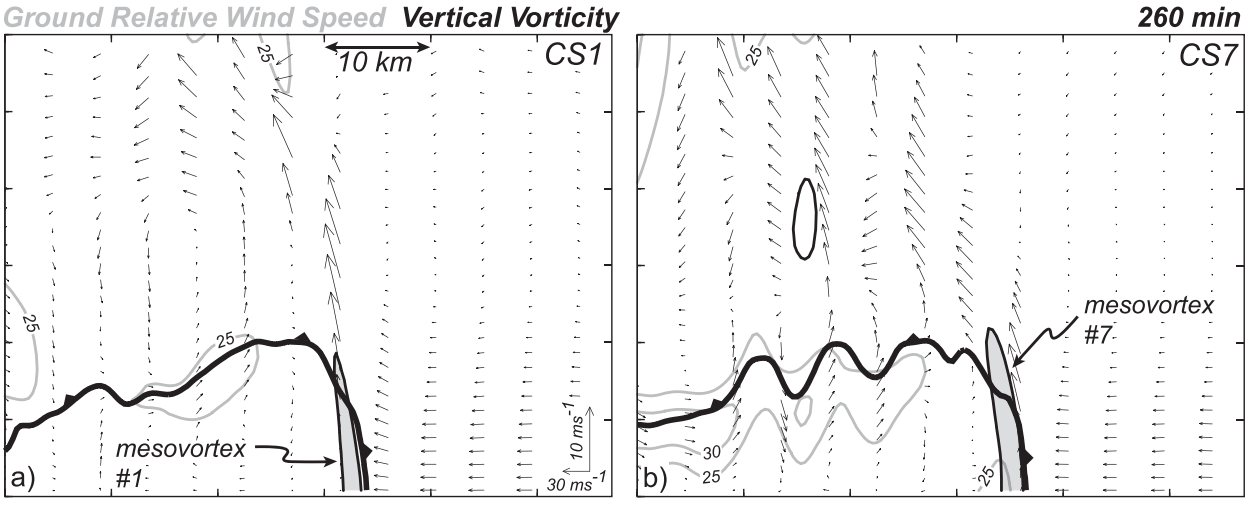

FIG. 11. As in Fig. 10, but that the cross sections are at 260 min. Cross-section locations are labeled and shown as dashed lines in Fig. 9e.

merged mesovortex is shown in Fig. 12b and appeared to be producing about 18–21 m s^{-1} of GRWS within the local maxima. The flow field without the mesovortex is shown in Fig. 12c and is generated by the RIJ that has descended to the surface. The descending RIJ appeared to be contributing approximately 25–31 m s^{-1} of flow within the local maxima of GRWS. The addition of the vortex flow in Fig. 12b with the RIJ in Fig. 12c roughly accounts for the total GRWS observed in Fig. 12a and thus, supports the hypothesis that the linear superposition of the vortex flow with the embedded RIJ creates the local maxima in near-surface GRWS. A similar result was observed with the weaker mesovortex 5 that produced 30 m s^{-1} of near-surface GRWS (Fig. 12a). The vortex flow accounted for approximately 10 m s^{-1} of the total while the weaker RIJ contributed about 20 m s^{-1}.

The same analysis was applied to the weaker mesovortex 7 located on the southern periphery of the gust front at 260 min (Fig. 13). A 25 m s^{-1} local GRWS maximum was observed on the western side of the mesovortex (Fig. 13a). The displacement of the GRWS maximum to the western side of the mesovortex was attributed to the vortex moving southward along the gust front at a speed of 13 m s^{-1}. Similar to the vortices in Fig. 12, however, the local maximum in GRWS (Fig. 13 a) was created by a linear superposition of the vortex (Fig. 13b) and translational (Fig. 13c) flows. The mesovortex contributed about 10 m s^{-1} of the total GRWS (Fig. 13b), while the system contributed about 15 m s^{-1} (Fig. 13c). These values are much weaker than for the merged mesovortex located near the bow echo apex. Interestingly, the vortex contribution of 10 m s^{-1} to the near-surface GRWS was similar for mesovortices 5 and 7 despite their differing locations along the gust front. The GRWS maximum associated with mesovortex 5 was larger because of the greater system flow observed closer to the stronger RIJ. For all mesovortices shown in Figs. 12 and 13, the mesovortex contribution to the GRWS maximum was less than the system contribution.

5. Summary and discussion

Quasi-idealized WRF simulations of the 10 June 2003 Saint Louis bow echo event observed during BAMEX and documented by Atkins et al. (2005) have been presented. The goal of this study was to better understand how environmental conditions and convective system processes affect the potential for mesovortices formed on the bow echo gust front to produce surface wind damage.

A control run was generated using a sounding representative of the environment that spawned the 10 June 2003 Saint Louis bow echo. Sensitivity experiments were performed that examined the impact of low-level (0–2.5 km) and deep (0–5 km) shear, Coriolis forcing, and cold-pool strength on mesovortex evolution. Mesovortex evolution was documented by calculating the circulation, maximum vertical vorticity, and the number of vertical vorticity centers observed at the lowest model grid level (81 m).

Stronger, more potentially damaging mesovortices formed when the low-level shear was nearly balanced by the horizontal vorticity produced by the cold pool. This balance resulted in deep, upright updrafts (Rotunno et al. 1988). Deep, upright updrafts created greater mesovortex stretching. Weaker low-level

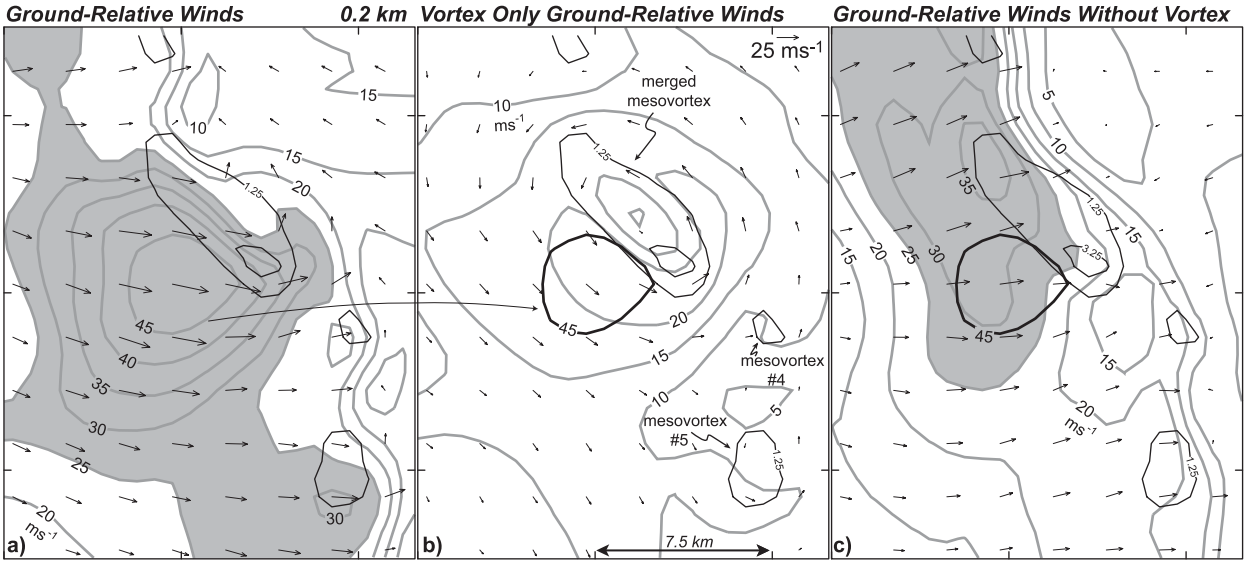

FIG. 12. (a) Decomposition of the total ground-relative winds into (b) the component produced by mesovortices and (c) the total ground-relative flow minus the mesovortices. In (a)–(c), the ground-relative wind speed (m s^{-1}) is contoured in gray and the respective wind field is shown with black vectors. Vertical vorticity ($\times 10^{-2}$ s^{-1}) is plotted with thin black lines. The 45 m s^{-1} ground-relative wind speed isotach in (a) is plotted in (b) and (c) as a thick black line.

sheared environments that allowed the convective system updraft to tilt significantly upshear produced fewer and weaker mesovortices. Mesovortex production was also delayed in the weaker shear simulations. These results are consistent with those observed by Weisman and Trapp (2003).

The deeper-shear simulations behaved in a similar manner as the low-level shear runs in that as the magnitude of deep shear decreased, mesovortex production was delayed and the mesovortices tended to be weaker. The amount of circulation produced in the first 4 h decreased as the deep-shear magnitude decreased.

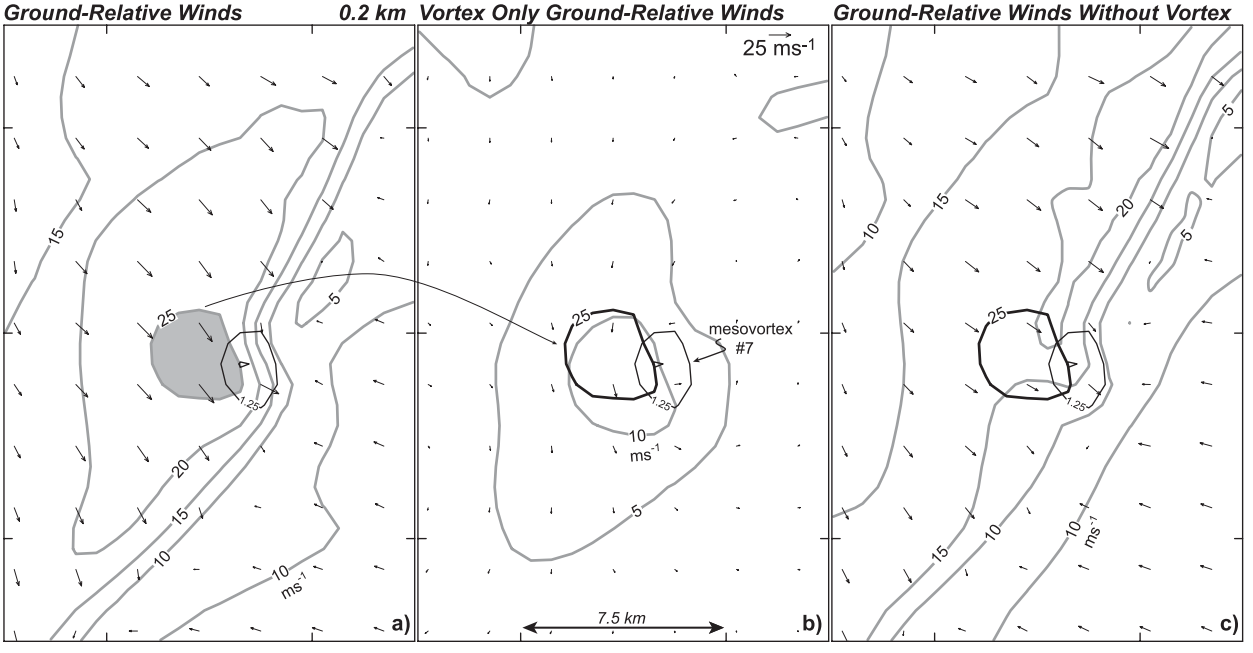

FIG. 13. As in Fig. 12, but that the analysis is centered on mesovortex 7 in Fig. 9e.

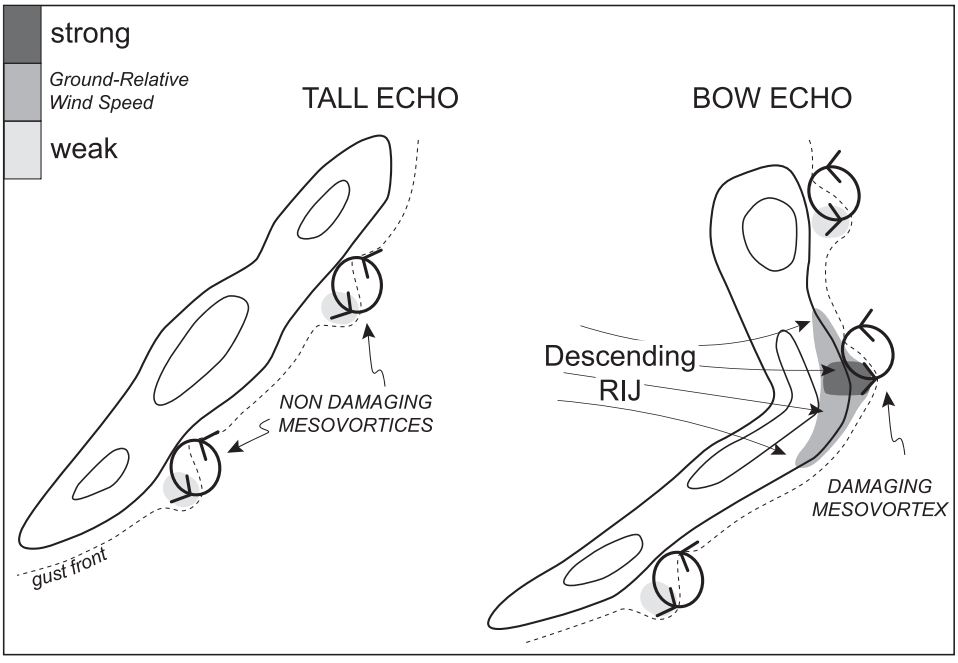

FIG. 14. Schematic diagram illustrating damaging and nondamaging mesovortices formed within a bow echo.

Circulation magnitudes were similar for all deep-shear runs after 4 h. Generally, the number of mesovortices decreased as the deep-shear magnitude became weaker.

Similar to the results of Trapp and Weisman (2003), increasing the magnitude of Coriolis forcing generated more low-level circulation. The increased low-level circulation was attributed to more intense and a larger number of mesovortices. Trapp and Weisman (2003) showed that convergence of planetary vorticity played an important role in the amplification of cyclonic mesovortices and acted to weaken their anticyclonic counterparts.

In the final set of sensitivity experiments, it was observed that less low-level circulation was produced as the cold-pool strength decreased. The decreased low-level circulation was attributed to fewer and somewhat weaker mesovortices. Weaker cold pools were also spatially smaller, providing fewer vortex generation sites along the gust front.

Within a particular sensitivity experiment, the magnitude of ground-relative wind speeds produced by bow echoes was observed to be quite variable. The strongest, and therefore, potentially most damaging mesovortices, were those that formed along the gust front that was locally being enhanced by a descending RIJ. Mesovortices that formed prior to RIJ genesis produced weaker ground-relative winds. Furthermore, mesovortices formed well north or south of the RIJ position were also observed to be much weaker. These results are consistent with observations of the 10 June 2003 Saint Louis bow echo documented by Atkins et al. (2005).

The strongest, potentially damaging surface winds within the simulated bow echoes, were found to be produced by a linear superposition of the vortex flow with the system flow within which it was embedded, shown in the schematic diagram in Fig. 14. This result is consistent with the damage survey and airborne Doppler radar analysis of a bow echo mesovortex discussed by Wakimoto et al. (2006b). They observed the strongest ground-relative winds on the southern periphery of an eastward-moving mesovortex that was embedded within the descending RIJ. Weaker near-surface GRWS were produced in the simulations by mesovortices formed prior to the emergence of the RIJ or with those located well north or south of the RIJ position. This result is consistent with damage survey and single-Doppler radar analyses presented by Atkins et al. (2005). The observation that a mesovortex alone may not be damaging is perhaps not surprising. Single-Doppler data presented by Atkins et al. (2005) showed that the vortex-relative radial velocities within the couplet are not particularly strong, often less than 17 m s^{-1}.

In summary, the results of the first part of this study suggest that the strongest and potentially most damaging near-surface GRWS produced by mesovortices would occur within a bow echo containing a strong cold pool that is nearly balanced by moderate to strong low-level

wind shear. Within the bow echo, the most damaging surface winds may be found on the southern periphery of a mesovortex that has formed along the portion of the gust front that is being enhanced by a descending RIJ.

The results reported herein are only valid for the generation of near-surface straight-line winds and not damage produced by tornadic mesovortices. Because of the coarse model resolution, it is not possible to understand how mesovortices may produce tornadoes in the simulations reported herein. Furthermore, it is not known if the results of this study are applicable to serial bow echoes (Johns and Hirt 1987) commonly observed in more strongly forced environments during the cool season. These issues are important problems that will be addressed in future research.

Acknowledgments. Research results presented in this paper were supported by the National Science Foundation under Grant ATM-0630445 and Vermont EPSCoR EPS-0236976. Graphics were created by the Read/Interpolate/Plot (RIP) software package created by Mark T. Stoelinga. Comments from three anonymous reviewers on an early version of this manuscript were greatly appreciated.

REFERENCES

Adlerman, E. J., and K. K. Droegemeier, 2002: Sensitivity of numerically simulated cyclic meso-cyclogenesis to variations in model physical and computational parameters. *Mon. Wea. Rev.,* **130,** 2671–2691.

Atkins, N. T., and M. St. Laurent, 2009: Bow echo mesovortices. Part II: Their genesis. *Mon. Wea. Rev.,* **137,** 1514–1532.

——, J. M. Arnott, R. W. Przybylinski, R. A. Wolf, and B. D. Ketcham, 2004: Vortex structure and evolution within bow echoes. Part I: Single-Doppler and damage analysis of the 29 June 1998 derecho. *Mon. Wea. Rev.,* **132,** 2224–2242.

——, C. S. Bouchard, R. W. Przybylinski, R. J. Trapp, and G. Schmocker, 2005: Damaging surface wind mechanism within the 10 June 2003 Saint Louis bow echo during BAMEX. *Mon. Wea. Rev.,* **133,** 2275–2296.

Burgess, D. W., and B. F. Smull, 1990: Doppler radar observations of a bow echo associated with a long-track severe windstorm. Preprints, *16th Conf. on Severe Local Storms,* Kananaskis Park, Alberta, Canada, Amer. Meteor. Soc., 203–208.

Davis, C., and Coauthors, 2004: The bow-echo and MCV experiment (BAMEX): Observations and opportunities. *Bull. Amer. Meteor. Soc.,* **85,** 1075–1093.

Evans, J. S., and C. A. Doswell, 2001: Examination of derecho environments using proximity soundings. *Wea. Forecasting,* **16,** 329–342.

Forbes, G. S., and R. M. Wakimoto, 1983: A concentrated outbreak of tornadoes, downbursts and microbursts, and implications regarding vortex classification. *Mon. Wea. Rev.,* **111,** 220–236.

Fujita, T. T., 1978: Manual of downburst identification for project Nimrod. Satellite and Mesometeorology Research Paper 156, Dept. of Geophysical Sciences, University of Chicago, 104 pp. [NTIS PB-286048.]

——, 1979: Objectives, operation, and results of project NIMROD. Preprints, *11th Conf. on Severe Local Storms,* Kansas City, MO, Amer. Meteor. Soc., 259–266.

——, 1981: Tornadoes and downbursts in the context of generalized planetary scales. *J. Atmos. Sci.,* **38,** 1511–1534.

——, and R. M. Wakimoto, 1981: Five scales of airflow associated with a series of downbursts of 16 July 1980. *Mon. Wea. Rev.,* **109,** 1438–1456.

Funk, T. W., K. E. Darmofal, J. D. Kirkpatrick, V. L. DeWald, R. W. Przybylinski, G. K. Schmocker, and Y.-J. Lin, 1999: Storm reflectivity and mesocyclone evolution associated with the 15 April 1994 squall line over Kentucky and southern Indiana. *Wea. Forecasting,* **14,** 976–993.

Johns, R. H., and W. D. Hirt, 1987: Derechos: Widespread convectively induced wind-storms. *Wea. Forecasting,* **2,** 32–49.

Jorgensen, D. P., and B. F. Smull, 1993: Mesovortex circulations seen by airborne Doppler radar within a bow-echo mesoscale convective system. *Bull. Amer. Meteor. Soc.,* **74,** 2146–2157.

——, and T. M. Weckwerth, 2003: Forcing and organization of convective systems. *Radar and Atmospheric Science: A Collection of Essays in Honor of David Atlas*, *Meteor. Monogr.,* No. 52, Amer. Meteor. Soc., 75–113.

Lafore, J.-P., and M. W. Moncrieff, 1989: A numerical investigation of the organization and interaction of the convective and stratiform regions of tropical squall lines. *J. Atmos. Sci.,* **46,** 521–544.

Lee, B. D., and R. B. Wilhelmson, 1997: The numerical simulation of non-supercell tornadogenesis. Part I: Initiation and evolution of pretornadic misocyclone and circulations along a dry outflow boundary. *J. Atmos. Sci.,* **54,** 32–60.

Lin, Y.-L., R. D. Farely, and H. D. Orville, 1983: Bulk parameterization of a snow field in a cloud model. *J. Climate Appl. Meteor.,* **22,** 1065–1092.

Orlanski, I., 1975: A rational subdivision of scales for atmospheric processes. *Bull. Amer. Meteor. Soc.,* **56,** 527–530.

Przybylinski, R. W., 1995: The bow echo: Observations, numerical simulations, and severe weather detection methods. *Wea. Forecasting,* **10,** 203–218.

Rotunno, R., J. B. Klemp, and M. L. Weisman, 1988: A theory for strong, long-lived squall lines. *J. Atmos. Sci.,* **45,** 463–485.

Schmidt, J. M., and W. R. Cotton, 1989: A high plains squall line associated with severe surface winds. *J. Atmos. Sci.,* **46,** 281–302.

Shea, D. J., and W. M. Gray, 1973: The hurricane's inner core region. I. Symmetric and asymmetric structure. *J. Atmos. Sci.,* **30,** 1544–1564.

Skamarock, W. C., J. B. Klemp, J. Dudhia, D. O. Gill, D. M. Barker, W. Wang, and J. G. Powers, 2005: A description of the Advanced Research WRF version 2. NCAR Tech. Note TN-468_STR, 88 pp. [Available from NCAR, P.O. Box 3000, Boulder, CO 80307.]

Trapp, R. J., and M. L. Weisman, 2003: Low-level mesovortices within squall lines and bow echoes. Part II: Their genesis and implications. *Mon. Wea. Rev.,* **131,** 2804–2823.

——, S. A. Tessendorf, E. S. Godfrey, and H. E. Brooks, 2005: Tornadoes from squall lines and bow echoes. Part I: Climatological distribution. *Wea. Forecasting,* **20,** 23–34.

Wakimoto, R. M., 1983: The West Bend, Wisconsin, storm of 4 April 1981: A problem in operational meteorology. *J. Climate Appl. Meteor.,* **22,** 181–189.

——, and P. G. Black, 1994: Damage survey of Hurricane Andrew and its relationship to the eyewall. *Bull. Amer. Meteor. Soc.,* **75,** 189–200.

——, H. V. Murphey, A. Nester, D. P. Jorgensen, and N. T. Atkins, 2006a: High winds generated by bow echoes. Part I: Overview of the Omaha bow echo 5 July 2003 storm during BAMEX. *Mon. Wea. Rev.,* **134,** 2793–2812.

——, ——, C. A. Davis, and N. T. Atkins, 2006b: High winds generated by bow echoes. Part II: The relationship between the mesovortices and damaging straight-line winds. *Mon. Wea. Rev.,* **134,** 2813–2829.

Weisman, M. L., 1992: The role of convectively generated rear-inflow jets in the evolution of long-lived mesoconvective systems. *J. Atmos. Sci.,* **49,** 1826–1847.

——, 1993: The genesis of severe, long-lived bow echoes. *J. Atmos. Sci.,* **50,** 645–670.

——, and R. J. Trapp, 2003: Low-level meso-vortices within squall lines and bow echoes. Part I: Overview and dependence on environmental shear. *Mon. Wea. Rev.,* **131,** 2779–2803.

Wheatley, D. M., R. J. Trapp, and N. T. Atkins, 2006: Radar and damage analysis of severe bow echoes observed during BAMEX. *Mon. Wea. Rev.,* **134,** 791–806.